Near-Field Mapping of Optical Fabry−Perot Modes in All-Dielectric Nanoantennas

Aleksandr Yu. Frolov,*[†] Niels Verellen,*[‡,§] Jiaqi Li,[§,‡] Xuezhi Zheng,[∥] Hanna Paddubrouskaya,[‡] Denitza Denkova,[⊥] Maxim R. Shcherbakov,[†] Guy A. E. Vandenbosch,[∥] Vladimir I. Panov,[†] Pol Van Dorpe,[§,‡] Andrey A. Fedyanin,[†] and Victor V. Moshchalkov[‡]

[†]Faculty of Physics, Lomonosov Moscow State University, 119991 Moscow, Russian Federation

[‡]INPAC-Institute for Nanoscale Physics and Chemistry and Department of Physics and Astronomy, KU Leuven, Celestijnenlaan 200 D, B-3001 Leuven, Belgium

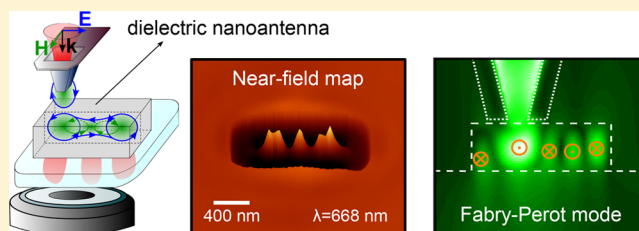[§]IMEC, Kapeldreef 75, B-3001 Leuven, Belgium

[∥]Department of Electrical Engineering (ESAT-TELEMIC), KU Leuven, Kasteelpark Arenberg 10, Heverlee, B-3001, Belgium

[⊥]ARC Centre of Excellence for Nanoscale BioPhotonics (CNBP), Macquarie University, Sydney, Australia

ⓢ *Supporting Information*

ABSTRACT: Subwavelength optical resonators and scatterers are dramatically expanding the toolset of the optical sciences and photonics engineering. By offering the opportunity to control and shape light waves in nanoscale volumes, recent developments using high-refractive-index dielectric scatterers gave rise to efficient flat-optical components such as lenses, polarizers, phase plates, color routers, and nonlinear elements with a subwavelength thickness. In this work, we take a deeper look into the unique interaction of light with rod-shaped amorphous silicon scatterers by tapping into their resonant modes with a localized subwavelength light source—an aperture scanning near-field probe. Our experimental configuration essentially constitutes a dielectric antenna that is locally driven by the aperture probe. We show how leaky transverse electric and magnetic modes can selectively be excited and form specific near-field distribution depending on wavelength and antenna dimensions. The probe's transmittance is furthermore enhanced upon coupling to the Fabry−Perot cavity modes, revealing all-dielectric nanorods as efficient transmitter antennas for the radiation of subwavelength emitters, in addition to constituting an elementary building block for all-dielectric metasurfaces and flat optics.

KEYWORDS: *All-dielectric nanophotonics, nanoantenna, scanning near-field optical microscopy, Fabry−Perot modes*

Resonant light interaction at the nanoscale with all-dielectric nanostructures finds applications in a wide range of nanophotonics research fields such as metasurfaces,[1−6] metamaterials,[7] color routers,[8,9] lab-on-a-chip biosensing,[10] nonlinear phenomena,[11,12] nanoantennas,[13] and all-optical switching.[14,15] The geometrical tunability of the magnetic and electric type resonances in all-dielectric nanostructures can easily be demonstrated by spectrally investigating their far-field scattering properties. Examples can be found for semiconductor nanowires (NWs)[16,17] and nanospheres.[18,19] While all-dielectric NWs, spherical, and cylindrical nanoparticles are well-studied, nanorods or nanoblocks, which are truncated NWs, lack a thorough experimental description. For light, a nanorod can constitute a three-dimensional Fabry−Perot (FP) cavity in which the electromagnetic fields resonantly couple into standing wave patterns. The impact of the geometrical tunability of these FP standing waves was demonstrated in terms of Purcell enhancement, photoluminescence and emission tailoring in finite NWs,[20] the transition of cavity FP modes into leaky waveguide modes and Mie modes,[21] and the tuning of the scattering efficiency in the visible range by means

of the lowest order FP mode in silicon (Si) nanoblocks.[22] By varying the aspect ratio of the dielectric nanocavities, it is even possible to overlap Mie and FP modes with different polarizations, leading to supercavity modes with an extremely high Q factor.[23] In addition, the interference of Mie-FP modes with electric dipoles was shown to result in multifrequency directional scattering,[24] while other recent work numerically predicts strong Fano resonances in the far-field scattering response of Si nanorods.[25] However, the clear observation of FP modes in nanoblocks and their cavity length dependence has only been possible for the lowest order FP mode using far-field techniques.[22] Higher order FP modes are only observed as minor spectral undulations in the scattering cross sections.[22] In addition, the mode-parity—which is determined by the either odd or even number of antinodes in the standing wave—determines whether a plane wave can couple to such a mode or
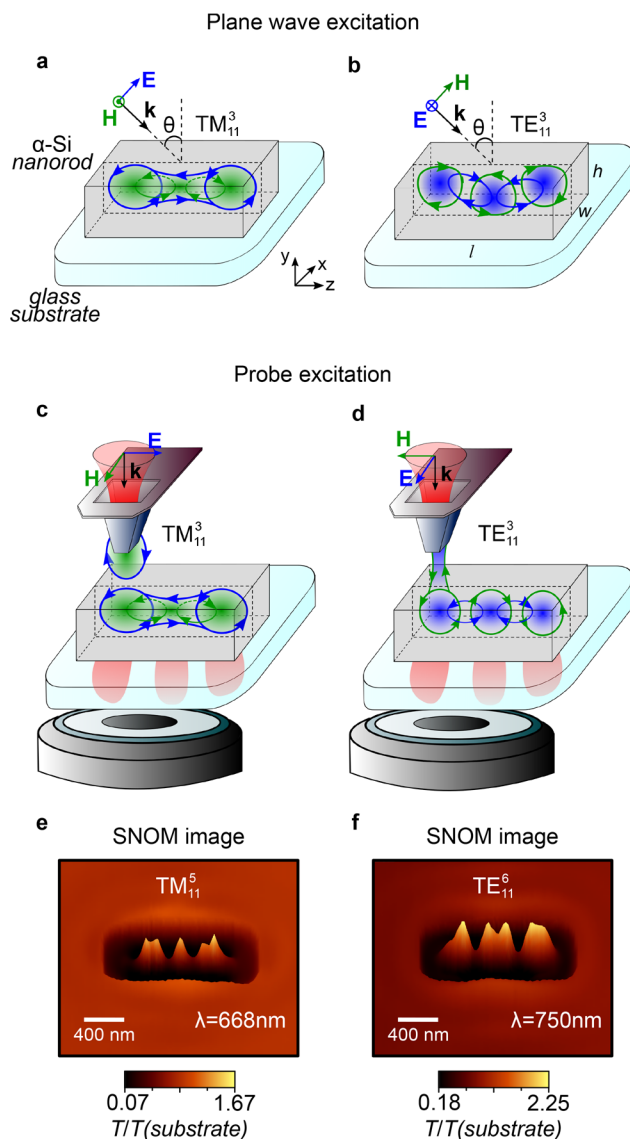
not. Introducing phase retardation by changing the angle of illumination modifies these parity dependent coupling selection rules.[21] To get more insight into the nature of cavity FP modes in all-dielectric nanorods in terms of the parity, standing wave antinode distribution, as well as near-field enhancement, near-field measurements are required. Moreover, for the design of coupled systems with, for example, precisely positioned quantum emitters near nanoantennas,[26] a well-controlled way to locally drive the cavity FP modes is highly desired.

Scanning near-field optical microscopy (SNOM) is one of the most powerful tools to directly visualize the near-field patterns of optical modes supported by nanophotonic structures with subdiffraction resolution.[27] For instance, different types of plasmonic nanoantenna structures ranging from nanorods,[28−30] nanodisks,[31] triangular nanoprisms,[32] and V-shapes[33] to loaded gap[34] and Yagi-Uda[35] antennas have been investigated by this technique. In the infrared range, even surface phonon polaritons can be imaged in linear antennas.[36] Among all-dielectric nanostructures, the near-field distribution of Mie and anapole modes of single Si-nanodisks,[37,38] magnetic field hotspots in a gap between Si-disk dimers[39] as well as the magnetic dipole scattering of a Si-sphere[40] were recently observed. When the scanning probe is hollow and has a subwavelength aperture at its apex, impinging light can tunnel through it and create a strongly localized light source.[41] The near fields of this aperture probe can, to a certain degree, be approximated by point dipole sources[42] and can in turn mimic the transient dipole radiation of real quantum emitters.

Here, we report on a near-field study of optical cavity FP modes supported by amorphous silicon (α-Si) nanorods. We illustrate how both polarized plane wave illumination and polarized local excitation by a near-field probe can launch TM and TE modes and form FP-like standing waves in a dielectric nanorod. Our samples consist of α-Si nanorods defined by electron beam lithography and reactive ion etching (RIE) on a glass substrate.[9] Experimental SNOM maps are analyzed and compared with full-field 3D finite difference time domain (FDTD) simulations of the full probe−antenna system. The good agreement between experimental and simulated profiles allows us to reveal the probe−antenna coupling mechanism. Next, the far-field extinction responses for nanorods of different lengths are matched with their corresponding simulated near-field distributions and experimental SNOM maps for TM and TE polarization. Additionally, we show that only weak spectral variations in the far-field response result from remarkably distinct changes in the near-field mode distribution. This further illustrates the power of SNOM in nanophotonics research. Lastly, we consider the α-Si nanorod as a transmitting antenna and evaluate the probe's transmittance enhancement upon coupling to the FP cavity modes. The current experimental study further confirms theoretical predictions regarding the interaction of a point electric dipole source with all-dielectric nanostructures[20,43,44] and opens new opportunities of tailoring near- and far-field light patterns.
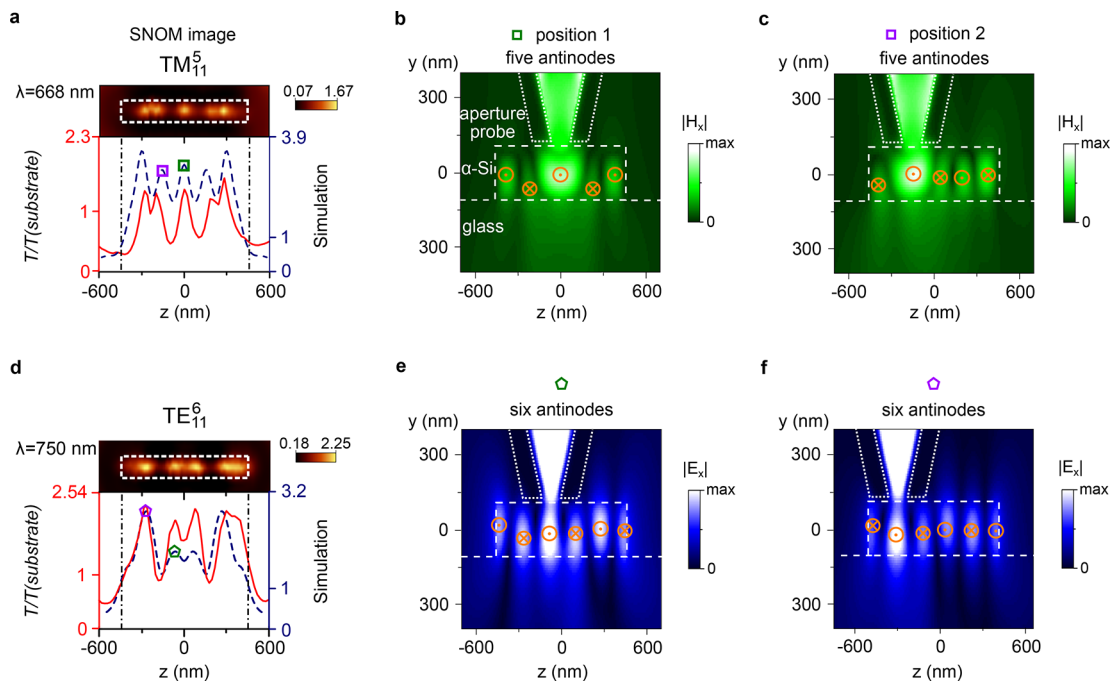
Results and Discussion. *Excitation and Mapping of FP Modes by Aperture SNOM.* FP modes supported by the nanorods with length l, width w, and thickness h are illustrated in Figure 1a,b. Transverse magnetic (TM, magnetic field is normal to the long axis of the nanorod) and transverse electric (TE, electric field is normal to the long axis of the nanorod) plane wave illumination is used for the excitation of FP modes inside the nanoantenna. More specifically, panels a and b illustrate the excitation of TM_{11}^3 and TE_{11}^3 FP modes,

Figure 1. Transverse magnetic (TM_{mj}^n) and transverse electric (TE_{mj}^n) Fabry−Perot modes supported by all-dielectric nanoantennas. (a,b) Illustration of the plane wave source excitation of TM_{mj}^n and TE_{mj}^n FP modes with the antinode number of n = 3 inside all-dielectric nanorods with length l, width w, and thickness h. (c,d) The illustration of the excitation and mapping of TM_{mj}^n and TE_{mj}^n FP modes by an aperture type SNOM probe (n = 3). The arrows indicate the directions of the **H** and **E** fields for a−d. (e,f) 3D representation of the experimental SNOM images of TM_{11}^5 and TE_{11}^6 FP modes in a nanorod with $l \times w \times h$ = 900 × 170 × 105 nm^3.

respectively. The mode indices m, j, and n in TM_{mj}^n and TE_{mj}^n indicate the number of magnetic field antinodes for TM illumination and electric field antinodes for TE illumination in the x, y, and z-directions, respectively.

Although the electromagnetic fields of the FP modes are localized to the volume and surface of the nanorods, the scanning near-field optical microscope operating in the illumination mode allows us to tap into them. The SNOM aperture probe effectively acts as a subwavelength localized light source that is able to locally excite FP modes in the nanorod. The schematic of the SNOM measurements is presented in Figure 1c,d. The SNOM probe is a SiO$_2$ pyramid coated by an Al layer with a thickness of 100 nm. The linearly polarized light

Figure 2. SNOM images and FDTD simulations of the aperture probe near-field coupling to TM_{11}^n and TE_{11}^n FP modes inside α-Si nanorod. (a,d) Top: 2D-SNOM image of TM_{11}^n and TE_{11}^n FP modes. (a,d) Bottom: red solid (blue dashed) curves indicate the experimental (simulated) SNOM transmission intensity at a cross-section through the middle of the SNOM image. FDTD simulations of $|H_x|$ field (b,c) and $|E_x|$ field (e,f) of TM_{11}^5 and TE_{11}^6 FP modes excited by SNOM probe. The probe positions correspond to the maximum values of the transmittance denoted by open squares and pentagons on the SNOM scan simulations. The plotted SNOM transmission T is normalized to the transmission through the substrate $T(\text{substrate})$ at the corresponding wavelength both for the experimental and simulated data. The white dotted lines show probe edges. The white dashed lines show the α-Si nanorod and glass substrate edges. The orange crosses and dots indicate the field direction. The dimensions of the nanorod are $l \times w \times h = 900 \times 170 \times 105$ nm^3.
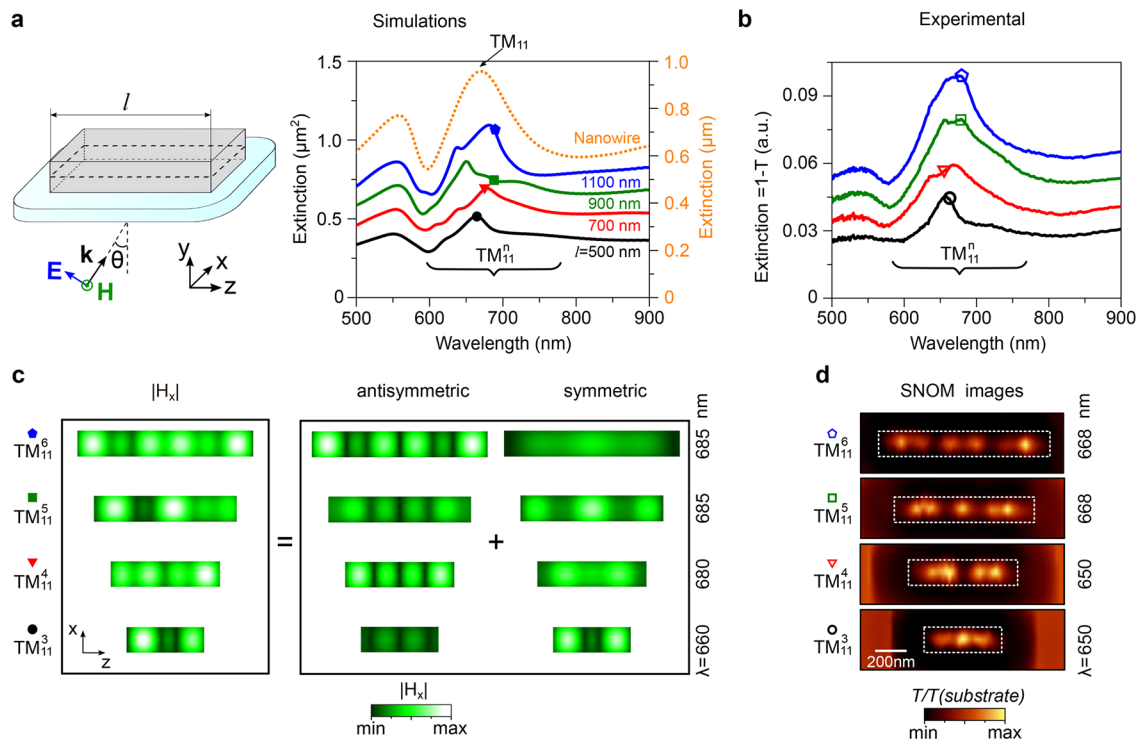
coming from a supercontinuum white light laser is focused by an objective through the pyramid on the apex of the probe. The polarization of the incident light is oriented along (TM polarization) or perpendicular to (TE polarization) the long axis of the nanorod. A strong evanescent near-field is created around the probe, which can excite TM_{mj}^n and TE_{mj}^n FP modes in the nanorod antenna. The light transmitted through the sample (T) is collected in the far-field by a 60× reflective objective (NA = 0.8), while the sample is scanned under the probe with a piezo stage (see Methods, Experimental Section). Figure 1e,f shows typical SNOM images of the α-Si nanorod supported by a glass substrate for TM and TE polarization, respectively (see Methods, Fabrication Section for fabrication details and Figure S1 in the Supporting Information for SEM and AFM characterization). The dimensions of the nanorod are $l \times w \times h = 900 \times 170 \times 105$ nm^3. The transmittance map has five peaks for TM polarization and six peaks for TE polarization within the nanorod area. In contrast, a uniform probe transmittance is observed on the glass substrate. The dark area around the nanorod corresponds to the decreased intensity of the transmitted light due to scattering when the probe is raised near the edges of the nanorod.

Full-field 3D FDTD simulations of the probe, nanorod, and substrate system were performed to unambiguously reveal the origin of the pronounced near-field patterns shown in Figure 1e,f. The results are summarized in Figure 2. First, in panels a and d, we show the simulated transmission (blue dashed curve) at different probe positions in combination with the experimental scan along the nanorod (red solid curve). Remarkably, the number and position of the transmission maxima (bright spots) is very well reproduced. By plotting the

zy cross-section in the simulation, we get access to the full field pattern that is generated inside the nanorod for the selected probe positions, indicated with the colored symbols in panels a and d. Standing waves are indeed launched by the probe at, respectively, the transverse magnetic field $|H_x|$ antinodes (transverse direction is along the x-axis) for TM polarization (panels b and c) and transverse electric field $|E_x|$ antinodes for TE polarization (panels e and f). Note that for this central yz cross-section, due to the symmetry, $|H_x| = |\mathbf{H}|$ for TM polarization and $|E_x| = |\mathbf{E}|$ for TE polarization. The simulated distributions of $|\mathbf{H}|$ (for TE) and $|\mathbf{E}|$ (for TM) fields present loops of either electric (for TM) or magnetic field (for TE) in the yz cross-section (see Figure S2 in the Supporting Information). For more information about the simulations refer to the Simulation Section.

Far-Field and Near-Field Characterization of FP Modes in α-Si Nanorods with Different Lengths. A dielectric nanorod as an optical nanoantenna is able to convert free space optical radiation into nanoscale localized electromagnetic energy, and vice versa, due to the excitation of FP modes. Therefore, the near-field distributions of these FP modes, as observed by SNOM, are expected to be similar to those obtained by far-field plane wave illumination, and to be linked to spectral features in the extinction response. The comparison of the SNOM images and near-field distributions of FP modes excited by plane wave illumination is shown in Figures 3 and 4 for TM and TE polarization, respectively. Panels a and b in Figures 3 and 4 show the simulated and experimental extinction (extinction = scattering + absorption) spectra of the nanorods with increasing length (see Methods, Simulation Section, and Experimental Section). To provide the excitation of FP
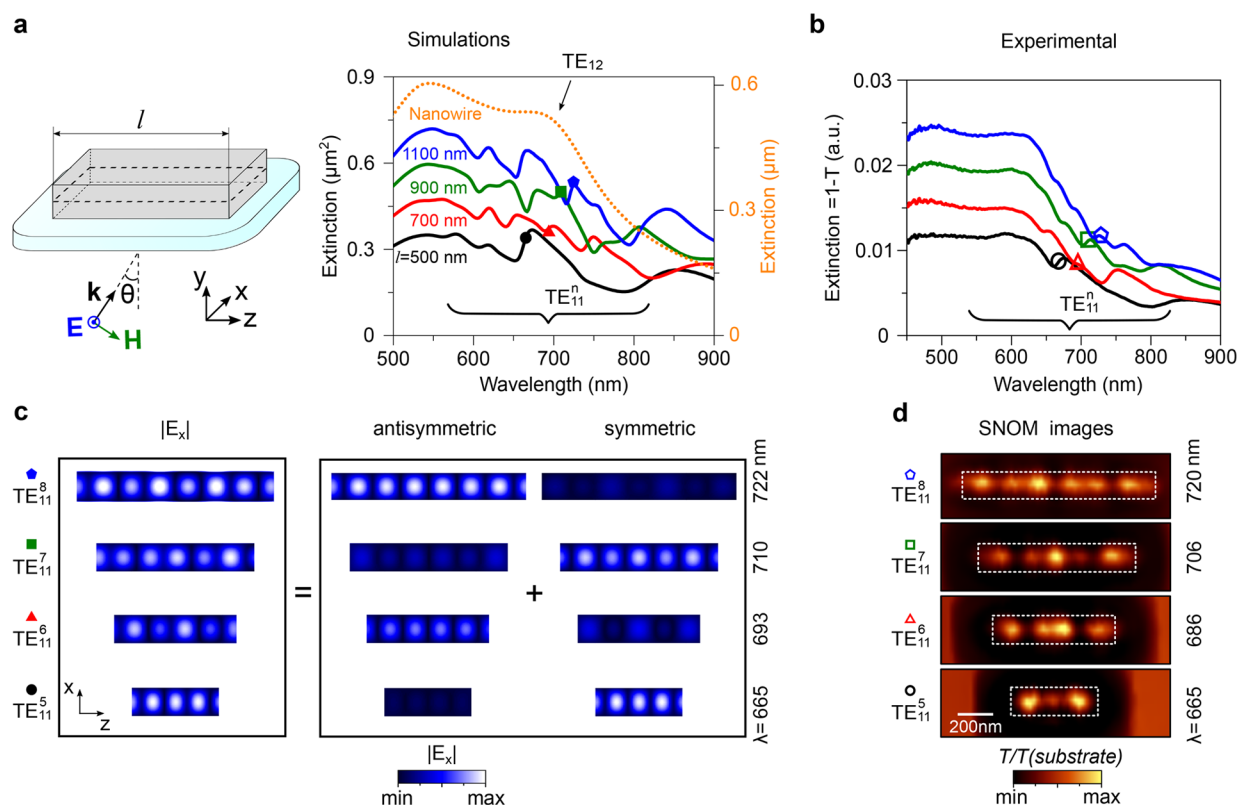
Figure 3. Near-field mapping of TM_{11}^n FP modes of dielectric nanorods obtained by SNOM and plane wave illumination. (a) Extinction spectra (TM polarization) of single α-Si nanorods with different length l = 500, 700, 900, and 1100 nm. The width and thickness equal w = 170 nm and h = 105 nm, respectively, for all nanorods. The sketch illustrates the simulation model. (b) Experimental extinction spectra of the α-Si nanorod arrays with l = 500, 700, 900, and 1100 nm. (c) Simulated distribution of the $|H_x|$ field and its decomposition to antisymmetric and symmetric components of TM_{11}^3–TM_{11}^6 FP modes inside single α-Si nanorods. The $|H_x|$ field was taken at the central xz cross-section of the nanorods as shown by a dashed line in panel a. The wavelengths at which the $|H_x|$ field distribution is plotted are marked with filled symbols on the simulated extinction spectra (a). The scale bar of the magnetic field value is the same for $|H_x|$, antisymmetric, and symmetric components. (d) Experimental SNOM images of TM_{11}^3–TM_{11}^6 modes of nanorods with different lengths. The white dotted box shows the edges of the nanorods. SNOM images were taken at the wavelengths which are marked with open symbols on the experimental extinction spectra (b).
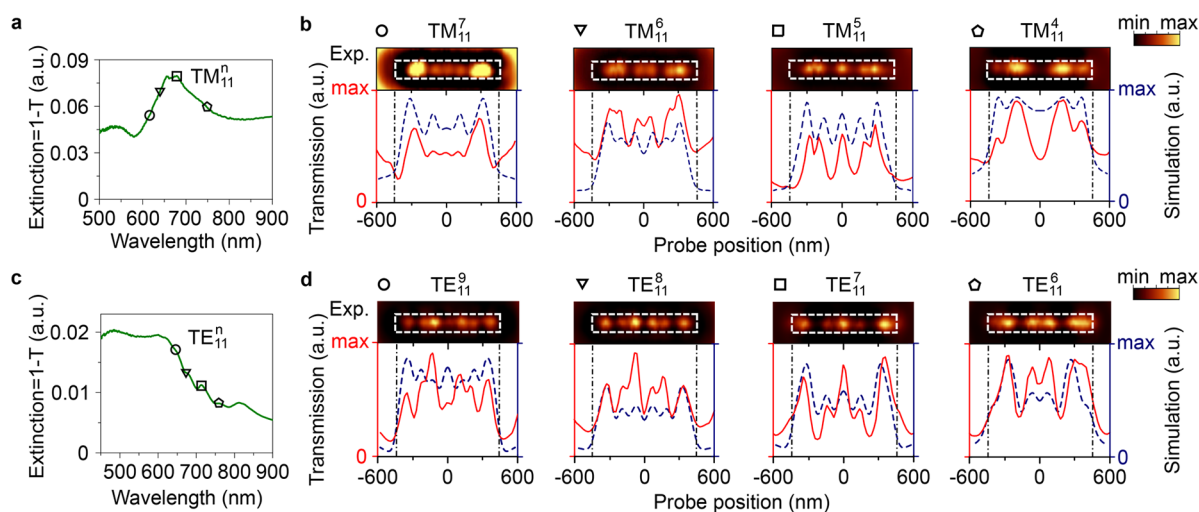
modes both with even and odd n, the symmetry of the system has to be broken to introduce sufficient field retardation along the nanorod.[45] We therefore used off-normal plane wave illumination incident from the substrate side at an angle of θ = 17° from the substrate normal (see sketch in Figure 3a). This angle corresponds to the average angle of incidence in the experiment (see Methods, Simulation and Experimental Sections, and Figure S9 showing the simulated extinction spectra for different angles within the range of the experimental illumination). For TM polarization, Figure 3a,b indicates a strong resonant peak located around λ = 670 nm both for nanorods and an infinite NW with the same thickness and width (dashed orange curve). The extinction simulations of the infinite NW were performed with normal plane wave illumination from the substrate side. The similarity of the extinction peaks for the nanorods and infinite NW results from the similarity of their resonant field pattern in the xy-plane. The extinction peaks around λ = 670 nm for nanorods and NW are associated with a TM_{11} field pattern in the xy-plane (see the distribution of the major $|H_x|$ component in the xy-plane in Figure S3, Supporting Information). The peak around λ = 540 nm corresponds to the higher order TM_{13} mode (see the field distribution in Figure S3, Supporting Information). The TM_{11} resonance occurs as a result of multiple interferences of the light reflecting from the facets of the nanorods or NW in the xy-plane.[46] The width and thickness of the nanorods or NW define the resonance condition for light in the xy plane, and increasing the length of the nanorods from l = 500 nm to l =

1100 nm does not change the spectral position of the extinction peaks at λ = 540 and 670 nm. The simulations of the extinction spectra (Figure 3a) show that the excitation of the cavity FP modes in the xz-plane introduces additional sharp spectral features with respect to the infinite NW, especially within the broad extinction peak at λ = 670 nm. These features are strongly affected by variations in the nanorod length. The experimental nanorod extinction spectra given in Figure 3b present similar additional peaks, in good agreement with the simulations. The equivalent results for TE polarization are shown in Figure 4a,b. The peak around λ = 650 nm (λ = 700 nm in the simulation) is associated with TE_{11} mode for nanorods and TE_{12} mode for the NW; see the distribution of the major $|E_x|$ component in the xy-plane for TE_{11} (λ = 700 nm) and higher-order mode TE_{13} (λ = 550 nm) in Figure S4, Supporting Information. Likewise for TM illumination, Figure 4a shows that the excitation of TE_{11}^n FP modes leads to the appearance of additional peaks inside TE_{12} band of the infinite NW for all investigated nanorod lengths.

Figures 3c and 4c depict the simulated standing wave patterns of the FP modes excited by a plane wave source in the central xz-plane cross section (dashed line in panel a). As mentioned earlier, to excite both odd and even modes, the plane wave in the simulations is incident under an angle in order to introduce the necessary phase retardation. However, the off-normal angle of illumination results in asymmetric standing wave patterns of the magnetic or electric field. To allow a fair comparison with the experimental SNOM maps,

Figure 4. Near-field mapping of TE_{11}^n FP modes of dielectric nanorods obtained by SNOM and plane wave illumination. (a) Extinction spectra (TE polarization) of single α-Si nanorods with different lengths l = 500, 700, 900, 1100 nm. The sketch illustrates the simulation model. The width and thickness equal w = 170 nm and h = 105 nm, respectively, for all nanorods. (b) Experimental extinction spectra of α-Si nanorod arrays with l = 500, 700, 900, and 1100 nm. (c) Simulated distribution of the $|E_x|$ field and its decomposition to antisymmetric and symmetric components of TE_{11}^5–TE_{11}^8 FP modes inside the single α-Si nanorods. The $|E_x|$ field was taken at the central xz cross-section of the nanorods as shown by a dashed line in panel a. The wavelengths at which the $|E_x|$ field distribution is plotted are marked with filled symbols on the simulated extinction spectra in panel a. The scale bar of the electric field value is the same for $|E_x|$, antisymmetric, and symmetric components. (d) Experimental SNOM images of TE_{11}^5–TE_{11}^8 modes of nanorods with different lengths. The white dotted box shows the edges of the nanorods. SNOM images were taken at the wavelengths which are marked with open symbols on the experimental extinction spectra (b).
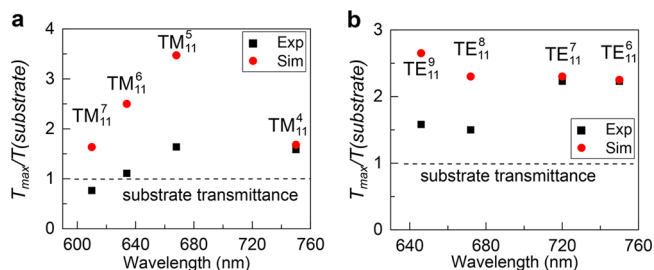

Figure 5. Spectral dependence of Fabry–Perot cavity modes inside α-Si nanorod. (a,c) The experimental extinction spectra of the array of α-Si nanorods with length l = 900 nm at TM and TE polarization. (b,d) Top row: the SNOM images of TM_{11}^7–TM_{11}^4 and TE_{11}^9–TE_{11}^6 FP modes of individual α-Si nanorods with l = 900 nm. Bottom graphs: red solid (blue dashed) curves indicate the experimental (simulated) SNOM transmission intensity at a cross-section through the middle of the SNOM image. SNOM images were taken at the wavelengths which are marked with open symbols on experimental extinction spectra (a,c). Both experimental (2D scans and red curves) and simulated (blue dashed curves) SNOM transmission intensity profiles are scaled individually for clarity. Absolute normalized transmission values allowing a direct comparison between the different modes can be found in the Supporting Information, Figure S10. Also the exact wavelengths corresponding to the different profiles are provided in the Supporting Information.

these asymmetric field patterns were decomposed into their symmetric and antisymmetric components using group representation theory.[47,48] More details are given in the Supporting Information. Doing so reveals the dominant mode contribution and its parity. For TM polarization, the distribution of the transverse magnetic field $|H_x|$ shows an increasing number of antinodes from three to six with the increasing length of the nanorods. The TM_{11}^3 mode evolves into TM_{11}^4, TM_{11}^5, and TM_{11}^6 modes upon increasing the nanorod length from $l = 500$ nm to $l = 1100$ nm. $|H_x|$ matches the dominant symmetric or antisymmetric part of the magnetic field for TM_{11}^3, TM_{11}^4, and TM_{11}^6. However, for TM_{11}^5, both the symmetric and the antisymmetric components have a considerable contribution to the $|H_x|$ field presenting five antinodes. Figure 3d shows that the number of bright spots in the experimental SNOM images are accurately reproduced by the number of the transverse magnetic field $|H_x|$ antinodes with even and odd parity in Figure 3c. In contrast to the simulated asymmetric near-field distributions obtained for plane wave illumination, the SNOM images yield symmetric patterns for which the mode parity can be deduced from the parity of the number of bright spots. The SNOM images predominantly map the $|H_x|$ component and the discrepancy with other field components for TM modes is demonstrated in Figure S5 (Supporting Information). Respectively, for TE polarization, Figure 4c shows that TE_{11}^5 mode with five electric field antinodes evolves into TE_{11}^6, TE_{11}^7, and TE_{11}^8 FP modes upon increasing the length. The bright spots in the SNOM images in Figure 4d are now reproduced by the antinodes of the transverse electric field $|E_x|$ in Figure 4c with even and odd parities. The SNOM images predominantly map the $|E_x|$ component, and the discrepancy with other field components for TE modes is demonstrated in Figure S6 (Supporting Information).

Spectral Dependence of FP Modes in α-Si Nanorods. Apart from investigating the mode evolution with changing antenna length, it is interesting to have a look at the spectral dependence for a fixed length and closely compare the near-field response with the far-field extinction response. Figure 5 shows the evolution of both TM_{11}^n and TE_{11}^n modes for a nanoantenna with $l = 900$ nm upon increasing the excitation wavelength. SNOM images were selected at the wavelengths corresponding to peaks in the extinction spectra as indicated in Figure 5a,c. We provide the experimental and simulated SNOM transmission intensity at a cross-section through the middle of the SNOM maps (bottom graphs in Figure 5b,d). With increasing the probe's illumination wavelength, TM_{11}^7, TM_{11}^6, TM_{11}^5, TM_{11}^4 and TE_{11}^9, TE_{11}^8, TE_{11}^7, TE_{11}^6 FP modes are revealed in the SNOM images. Note that for TM_{11}^7 mode, Figure 5b, we expect to see seven antinodes (bright spots). However, the spatial resolution of the probe is limited by its aperture diameter of 100 nm, and the antinodes at the edges of the nanorod cannot be resolved. Consequently, only five spots are observed. Overall, the experimental profiles correspond very well to the simulations. Although some variation in relative peak intensities is observed, the number of antinodes—and hence the mode number—as well as their positions are accurately reproduced. Remarkably, a very rich variety of well-defined standing-wave near-field patterns is revealed in the SNOM measurements, despite the fact that the corresponding extinction spectra only indicate a weakly varying far-field response. This further underpins the importance of near-field studies in the field of nanophotonics.

Enhancement of Transmission through the Aperture SNOM Probe. It was recently numerically predicted that dielectric nanoparticles or finite NWs are able to direct light of a localized point dipole through the excitation of Mie or FP modes.[20,43,44] The aperture probe in our experiments can effectively be considered as a localized light source mimicking a point dipole source.[42,49] The SNOM scans in Figure 1e,f show how the transmitted light intensity at the bright spots inside the antennas can be higher as compared to transmittance through the bare glass substrate. This reflects an inhomogeneous enhancement of the transmittance of the SNOM aperture probe in forward direction when the probe excites the antenna FP modes. Figure 6a,b shows the experimental ratio (black

Figure 6. Enhancement of the probe transmittance at the excitation of FP modes inside a α-Si nanoantenna as observed by a fixed NA objective. (a) Excitation of TM_{11}^n FP modes. (b) Excitation of TE_{11}^n FP modes. T_{max}(nanorod) is an average of two SNOM intensity values inside nanorod taken at two bright spots with highest intensity inside the nanorod. T(substrate) is the transmission value for the probe located directly on the substrate glass surface. The dimensions of the nanoantenna are $l \times w \times h = 900 \times 170 \times 105$ nm^3.

squares) of the transmittance detected at the bright spots T_{max}(nanorod), that is, where the FP modes are excited, and the transmittance at the substrate T(substrate), as calculated from the SNOM images of the nanorod with $l = 900$ nm in Figures 5b,d. The coupling of the probe near-field to the FP modes enhances the probe transmittance in the forward direction. The maximum value of the enhancement equals T_{max}/T(substrate) = 1.7 and T_{max}/T(substrate) = 2.1 when, respectively, TM_{11}^5 and TE_{11}^6 modes are excited. Simulated values (red dots) are included in Figure 6a,b. The experimental T_{max}/T(substrate) values are in good agreement with the simulations for $\lambda > 700$ nm. The mismatch at $\lambda < 700$ nm can be attributed to an underestimation of the absorption losses in this wavelength range in the simulations (see Supporting Information, Figure S8). It should be noted that the simulated far-field radiation pattern in forward direction of TM and TE FP modes excited by the SNOM probe shows that indeed most of the scattered light is collected by the collection objective in the experimental setup (see Figure S11 in the Supporting Information).

Conclusions. We have applied the aperture type scanning near-field optical microscopy (SNOM) technique to map the near-field of Fabry−Perot optical modes supported by individual α-Si nanorods. In stark contrast to their mostly uneventful far-field extinction response, a rich variety of distinct patterns of bright spots—corresponding to enhanced transmittance of the probe excitation—are observed in the near-field scans. As expected for a Fabry−Perot cavity, the distribution and number of these bright spots are found to strongly depend on both the excitation wavelength and the length of the dielectric antenna cavity. Decomposing the simulated field profiles into their symmetric and antisymmetric components

using group theory, in combination with far-field extinction spectroscopy measurements, allowed us to unambiguously link the SNOM maps to standing wave resonances of TM and TE polarized leaky waveguide modes supported by the silicon nanorods. Due to the localized dipole-like nature of the aperture-probe, both odd and even parity TM and TE modes are easily addressed. Odd parity Fabry−Perot modes are characterized by an odd number of bright near-field spots, while even parity modes are recognized by an even number. Interestingly, the strong coupling with TM and TE FP modes results in an enhancement of the probe's transmittance in the forward direction up to a factor of 2, illustrating how these high refractive index nanorods can effectively act as optical transmitter antennas. The presented optical near-field investigation of all-dielectric nanorod antennas will contribute to the further development of directional optical energy transfer at the nanoscale, radiation control of quantum emitters,[26,50,51] all-dielectric metasurfaces, and flat optics.

Methods. *Fabrication Section.* In the present work, we investigate dielectric nanoantennas made from amorphous silicon (α-Si). A layer of 105 nm α-Si was deposited on a glass substrate using plasma enhanced chemical vapor deposition (PECVD). Different arrays of nanorod antennas were subsequently patterned using e-beam lithography and inductively coupled plasma (ICP) SF6/CF4 dry etching according to our previously reported recipe.[9] The α-Si has a high refractive index of 4.0 and a low extinction coefficient k of 0.086 at $\lambda = 600$ nm. In the near infrared at 700 nm, k reduces to 10^{-5}. The pitch of the nanorod arrays is 4 μm. This ensures minimal near- and far-field coupling between the rods. Both SNOM measurements of single nanorods and far-field extinction spectroscopy were performed on the same samples.

Simulation Section. Simulations were performed using the finite-difference time-domain (FDTD) method.[52] For simulations with the plane wave excitation, a total-field scattered-field source was used. From these simulations, the extinction spectra as well as the field profiles were obtained. The experimental refractive index data of the α-Si, as determined by ellipsometry, was used, and the refractive index of the glass substrate was taken as 1.52. To match the experimental spectroscopy conditions, the angle of incidence of the plane wave was set to 17°. This angle equals the average angle of the light cone impinging on the nanorod arrays in the measurements.

In the simulations which include the presence of the SNOM probe, the probe was modeled as a hollow SiO$_2$ pyramid coated with a 100 nm thick Al layer. The diameter of the hole at the apex of the pyramid equals 100 nm. The distance between the apex of the probe and the nanorod is 10 nm. For excitation, a plane wave source is positioned inside the pyramid. The polarization of the plane wave source was oriented either along (TM polarization) or perpendicular to (TE polarization) the long axis of nanorods. The probe was moved with steps of 10 nm along the nanorod long axis (Figure 1c,d), while the transmitted light intensity was recorded. To better simulate the experimental conditions, the NA of the collection objective was taken into account by calculating the transmission intensity through a rectangular surface spanning the same collection angle.[29]

Experimental Section. *SNOM Measurements.* Near-field measurements were performed with an aperture type scanning near-field optical microscope (WITec, alfa300 s[53]) in transmission illumination mode. The probe consists of a hollow

SiO$_2$ pyramid coated with 100 nm of Al. A small hole of 100 nm in diameter is etched at the pyramid's apex. This subwavelength hole provides the optical resolution below the diffraction limit. A supercontinuum white light laser (NKT Photonics, Koheras SuperK Extreme Standard) with an acousto-optical tunable filter (AOTF) was used as the light source. The AOTF selects simultaneously up to eight wavelength channels from the spectrum of the supercontinuum. The spectral width of each channel is around 10−20 nm. After the passing through a polarizer, the light is focused on the apex of the probe by an objective with 20× magnification, NA = 0.4. The long axis of the nanorods was either parallel or perpendicular to the light polarization. The light transmitted through the aperture probe and the nanorod was collected in the far-field by a reflective objective with NA = 0.8 and delivered to a spectrometer (Princeton Instruments) equipped with a Si CCD camera. The sample scanning was performed in atomic force microscopy contact mode.

Extinction Measurements. Extinction measurements were conducted on the arrays of nanorods (see Fabrication Section). Experimental extinction spectra where obtained with a Fourier transform infrared (FTIR) spectrometer microscope (Bruker Vertex 80v and Hyperion) equipped with 15× magnification Cassegrain condensers for excitation and collection in transmission.[9,45] After passing through a polarizer, the light is focused by the bottom Cassegrain condenser on the nanorod arrays at angles between 10° and 24°. The central angle of $\theta = 17$° equals the angle used in the FDTD simulations. The top condenser collected the light transmitted through the array. Simulations of the FP modes in the range of the experimental angles show minor changes in their far- and near-field response related to the excitation efficiency of even parity modes (see Figure S9 in the Supporting Information). These modes especially are sensitive to the phase retardation of the asymmetric illumination conditions.

■ ASSOCIATED CONTENT

Ⓢ Supporting Information

The Supporting Information is available free of charge on the ACS Publications website at DOI: 10.1021/acs.nanolett.7b03624.

> SEM and AFM characterization of α-Si nanorods (Figure S1); FDTD simulations of the probe near-field coupling with **E** field component for TM$_{11}^5$ and **H** field for TE$_{11}^6$ (Figure S2); comparison of the field pattern of TM$_{mj}^n$ and TE$_{mj}^n$ FP modes of the nanorods in the transverse (xy) plane and TM$_{mj}$ and TE$_{mj}$ modes of the infinite nanowire (NW) (Figure S3 and S4); the simulations of the all components of the **H** and **E** field of TM FP modes excited by plane wave source (Figure S5); the simulations of the all components of the **E** and **H** of TE FP modes excited by plane wave source (Figure S6); a group representation theory based approach for field decomposition (Figure S7); comparison of the α-Si nanorod scattering and absorption cross sections (Figure S8); the simulated extinction cross-section spectra and near-field patterns with variation of the incident angle (Figure S9); the normalized values of the experimental and simulated SNOM transmission (Figure S10); the simulations of the far-field radiation patterns of TM and TE FP modes excited by SNOM probe (Figure S11) (PDF)

■ AUTHOR INFORMATION

Corresponding Authors
*E-mail: frolov@nanolab.phys.msu.ru.
*E-mail: niels.verellen@imec.be.

ORCID
Aleksandr Yu. Frolov: 0000-0003-0988-1361
Andrey A. Fedyanin: 0000-0003-4708-6895

Author Contributions
A.Y.F. and N.V. contributed equally to this work.

Notes
The authors declare no competing financial interest.

■ ACKNOWLEDGMENTS

■ REFERENCES

(1) Kuznetsov, A. I.; Miroshnichenko, A. E.; Brongersma, M. L.; Kivshar, Y. S.; Luk'yanchuk, B. *Science* **2016**, *354*, aag2472.
(2) Lin, D.; Fan, P.; Hasman, E.; Brongersma, M. L. *Science* **2014**, *345*, 298−302.
(3) Arbabi, A.; Horie, Y.; Bagheri, M.; Faraon, A. *Nat. Nanotechnol.* **2015**, *10*, 937−943.
(4) Kamali, S. M.; Arbabi, E.; Arbabi, A.; Horie, Y.; Faraon, A. *Laser Photon. Rev.* **2016**, *10*, 1002−1008.
(5) Kruk, S.; Hopkins, B.; Kravchenko, I. I.; Miroshnichenko, A.; Neshev, D. N.; Kivshar, Y. S. *APL Photonics* **2016**, *1*, 030801.
(6) Chong, K. E.; Staude, I.; James, A.; Dominguez, J.; Liu, S.; Campione, S.; Subramania, G. S.; Luk, T. S.; Decker, M.; Neshev, D. N.; Brener, I.; Kivshar, Y. S. *Nano Lett.* **2015**, *15*, 5369−5374.
(7) Jahani, S.; Jacob, Z. *Nat. Nanotechnol.* **2016**, *11*, 23−36.
(8) Yu, N.; Capasso, F. *Nat. Mater.* **2014**, *13*, 139−150.
(9) Li, J.; Verellen, N.; Vercruysse, D.; Bearda, T.; Lagae, L.; Van Dorpe, P. *Nano Lett.* **2016**, *16*, 4396−4403.
(10) Yavas, O.; Svedendahl, M.; Dobosz, P.; Sanz, V.; Quidant, R. *Nano Lett.* **2017**, *17*, 4421−4426.
(11) Shcherbakov, M. R.; Neshev, D. N.; Hopkins, B.; Shorokhov, A. S.; Staude, I.; Melik-Gaykazyan, E. V.; Decker, M.; Ezhov, A. A.; Miroshnichenko, A. E.; Brener, I.; Fedyanin, A. A.; Kivshar, Y. S. *Nano Lett.* **2014**, *14*, 6488−6492.
(12) Shcherbakov, M. R.; Shorokhov, A. S.; Neshev, D. N.; Hopkins, B.; Staude, I.; Melik-Gaykazyan, E. V.; Ezhov, A. A.; Miroshnichenko, A. E.; Brener, I.; Fedyanin, A. A.; Kivshar, Y. S. *ACS Photonics* **2015**, *2*, 578−582.
(13) Krasnok, A. E.; Miroshnichenko, A. E.; Belov, P. A.; Kivshar, Y. S. *Opt. Express* **2012**, *20*, 20599−20604.
(14) Shcherbakov, M. R.; Vabishchevich, P. P.; Shorokhov, A. S.; Chong, K. E.; Choi, D.-Y.; Staude, I.; Miroshnichenko, A. E.; Neshev, D. N.; Fedyanin, A. A.; Kivshar, Y. S. *Nano Lett.* **2015**, *15*, 6985−6990.
(15) Shcherbakov, M. R.; Liu, S.; Zubyuk, V. V.; Vaskin, A.; Vabishchevich, P. P.; Keeler, G.; Pertsch, T.; Dolgova, T. V.; Staude, I.; Brener, I.; Fedyanin, A. A. *Nat. Commun.* **2017**, *8*, 17.
(16) Cao, L.; Fan, P.; Barnard, E. S.; Brown, A. M.; Brongersma, M. L. *Nano Lett.* **2010**, *10*, 2649−2654.
(17) Brönstrup, G.; Jahr, N.; Leiterer, C.; Csáki, A.; Fritzsche, W.; Christiansen, S. *ACS Nano* **2010**, *4*, 7113−7122.
(18) Kuznetsov, A. I.; Miroshnichenko, A. E.; Fu, Y. H.; Zhang, J.; Luk'yanchuk, B. *Sci. Rep.* **2012**, *2*, 492.
(19) Evlyukhin, A. B.; Novikov, S. M.; Zywietz, U.; Eriksen, R. L.; Reinhardt, C.; Bozhevolnyi, S. I.; Chichkov, B. N. *Nano Lett.* **2012**, *12*, 3749−3755.
(20) Paniagua-Domínguez, R.; Grzela, G.; Rivas, J. G.; Sánchez-Gil, J. A. *Nanoscale* **2013**, *5*, 10582−10590.
(21) Traviss, D. J.; Schmidt, M. K.; Aizpurua, J.; Muskens, O. L. *Opt. Express* **2015**, *23*, 22771−22787.
(22) Ee, H.-S.; Kang, J.-H.; Brongersma, M. L.; Seo, M.-K. *Nano Lett.* **2015**, *15*, 1759−1765.
(23) Rybin, M. V.; Koshelev, K. L.; Sadrieva, Z. F.; Samusev, K. B.; Bogdanov, A. A.; Limonov, M. F.; Kivshar, Y. S. *arXiv*:1706.02099, **2017**.
(24) Yang, Y.; Miroshnichenko, A. E.; Kostinski, S. V.; Odit, M.; Kapitanova, P.; Qiu, M.; Kivshar, Y. S. *Phys. Rev. B: Condens. Matter Mater. Phys.* **2017**, *95*, 165426.
(25) Abujetas, D. R.; Mandujano, M. A. G.; Méndez, E. R.; Sánchez-Gil, J. A. *ACS Photonics* **2017**, *4*, 1814−1821.
(26) Bouchet, D.; Mivelle, M.; Proust, J.; Gallas, B.; Ozerov, I.; Garcia-Parajo, M. F.; Gulinatti, A.; Rech, I.; De Wilde, Y.; Bonod, N.; Krachmalnicoff, V.; Bidault, S. *Phys. Rev. Appl.* **2016**, *6*, 064016.
(27) Rotenberg, N.; Kuipers, L. *Nat. Photonics* **2014**, *8*, 919−926.
(28) Dorfmüller, J.; Vogelgesang, R.; Weitz, R. T.; Rockstuhl, C.; Etrich, C.; Pertsch, T.; Lederer, F.; Kern, K. *Nano Lett.* **2009**, *9*, 2372−2377.
(29) Denkova, D.; Verellen, N.; Silhanek, A. V.; Valev, V. K.; Van Dorpe, P.; Moshchalkov, V. V. *ACS Nano* **2013**, *7*, 3168−3176.
(30) Okamoto, H.; Imura, K. *J. Phys. Chem. Lett.* **2013**, *4*, 2230−2241.
(31) Esteban, R.; Vogelgesang, R.; Dorfmüller, J.; Dmitriev, A.; Rockstuhl, C.; Etrich, C.; Kern, K. *Nano Lett.* **2008**, *8*, 3155−3159.
(32) Rang, M.; Jones, A. C.; Zhou, F.; Li, Z.-Y.; Wiley, B. J.; Xia, Y.; Raschke, M. B. *Nano Lett.* **2008**, *8*, 3357−3363.
(33) Bohn, B. J.; Schnell, M.; Kats, M. A.; Aieta, F.; Hillenbrand, R.; Capasso, F. *Nano Lett.* **2015**, *15*, 3851−3858.
(34) Schnell, M.; García-Etxarri, A.; Huber, A.; Crozier, K.; Aizpurua, J.; Hillenbrand, R. *Nat. Photonics* **2009**, *3*, 287−291.
(35) Dorfmüller, J.; Dregely, D.; Esslinger, M.; Khunsin, W.; Vogelgesang, R.; Kern, K.; Giessen, H. *Nano Lett.* **2011**, *11*, 2819−2824.
(36) Alfaro-Mozaz, F. J.; Alonso-González, P.; Vélez, S.; Dolado, I.; Autore, M.; Mastel, S.; Casanova, F.; Hueso, L. E.; Li, P.; Nikitin, A. Y.; Hillenbrand, R. *Nat. Commun.* **2017**, *8*, 15624.
(37) Habteyes, T. G.; Staude, I.; Chong, K. E.; Dominguez, J.; Decker, M.; Miroshnichenko, A.; Kivshar, Y.; Brener, I. *ACS Photonics* **2014**, *1*, 794−798.
(38) Miroshnichenko, A. E.; Evlyukhin, A. B.; Yu, Y. F.; Bakker, R. M.; Chipouline, A.; Kuznetsov, A. I.; Luk'yanchuk, B.; Chichkov, B. N.; Kivshar, Y. S. *Nat. Commun.* **2015**, *6*, 8069.
(39) Bakker, R. M.; Permyakov, D.; Yu, Y. F.; Markovich, D.; Paniagua-Domínguez, R.; Gonzaga, L.; Samusev, A.; Kivshar, Y.; Luk'yanchuk, B.; Kuznetsov, A. I. *Nano Lett.* **2015**, *15*, 2137−2142.
(40) Permyakov, D.; Sinev, I.; Markovich, D.; Ginzburg, P.; Samusev, A.; Belov, P.; Valuckas, V.; Kuznetsov, A. I.; Luk'yanchuk, B. S.; Miroshnichenko, A. E.; Neshev, D. N.; Kivshar, Y. S. *Appl. Phys. Lett.* **2015**, *106*, 171110.
(41) Hecht, B.; Sick, B.; Wild, U. P.; Deckert, V.; Zenobi, R.; Martin, O. J.; Pohl, D. W. *J. Chem. Phys.* **2000**, *112*, 7761−7774.
(42) Colas des Francs, G.; Girard, C.; Weeber, J.-C.; Dereux, A. *Chem. Phys. Lett.* **2001**, *345*, 512−516.
(43) Rolly, B.; Stout, B.; Bonod, N. *Opt. Express* **2012**, *20*, 20376−20386.
(44) Staude, I.; Miroshnichenko, A. E.; Decker, M.; Fofang, N. T.; Liu, S.; Gonzales, E.; Dominguez, J.; Luk, T. S.; Neshev, D. N.; Brener, I.; Kivshar, Y. S. *ACS Nano* **2013**, *7*, 7824−7832.

(45) Verellen, N.; López-Tejeira, F.; Paniagua-Domínguez, R.; Vercruysse, D.; Denkova, D.; Lagae, L.; Van Dorpe, P.; Moshchalkov, V. V.; Sánchez-Gil, J. A. *Nano Lett.* **2014**, *14*, 2322−2329.

(46) Landreman, P. E.; Chalabi, H.; Park, J.; Brongersma, M. L. *Opt. Express* **2016**, *24*, 29760−29772.

(47) Zheng, X.; Verellen, N.; Vercruysse, D.; Volskiy, V.; Van Dorpe, P.; Vandenbosch, G. A. E.; Moshchalkov, V. V. *IEEE Trans. Antennas Propag.* **2015**, *63*, 1589−1602.

(48) Tinkham, M. *Group Theory and Quantum Mechanics*; Dover Publications, 2003; pp 18−48.

(49) le Feber, B.; Rotenberg, N.; Kuipers, L. *Nat. Commun.* **2015**, *6*, 6695.

(50) Albella, P.; Poyli, M. A.; Schmidt, M. K.; Maier, S. A.; Moreno, F.; Sáenz, J. J.; Aizpurua, J. *J. Phys. Chem. C* **2013**, *117*, 13573−13584.

(51) Curto, A. G.; Volpe, G.; Taminiau, T. H.; Kreuzer, M. P.; Quidant, R.; van Hulst, N. F. *Science* **2010**, *329*, 930−933.

(52) Lumerical FDTD Solutions. http://www.lumerical.com, 2017.

(53) WITec Wissenschaftliche Instrumente und Technologie GmbH. http://www.witec.de, 2017.